

# Effects of dissipation in reservoir computing using a spin qubit array

Shion Mifune and Tetsufumi Tanamoto

*Department of Information and Electronic Engineering,  
Teikyo University, Toyosatodai, Utsunomiya 320-8511, Japan*

Taro Kanao

*Computer Science and Engineering Course, College of Engineering,  
Shibaura Institute of Technology, Toyosu, Koto-ku, Tokyo 135-8548, Japan*

Reservoir computing (RC) is one of the hottest research topic as an application of many physical devices because the device characteristics can be used directly in computing sequences. Quantum RC is also a promising candidate for application in small-number qubit systems. Here, we propose a quantum RC based on the spin qubit system that reflects the status of the spin qubits in experiments comprising a one-dimensional qubit array. Spin qubits are coupled via the Heisenberg interaction, and data sequences are inputted to one of the spin qubits via pulsed rotations. By introducing dissipation, we obtained a relatively good performance in the quantum RC.

## I. INTRODUCTION

Spin qubits are promising platforms for quantum-computing devices. Since the proposal of Loss and DiVincenzo<sup>1</sup>, various theories have been proposed and many experiments have been conducted. GaAs systems were used in the early stages of the experiments, and the use of Si-based spin qubits has now become mainstream in experiments aimed at seamless fusion to the conventional silicon computers. The target architecture of qubits is the surface code consisting of a two-dimensional qubit array<sup>2</sup>, for which many proposals have been made<sup>3-5</sup>. However, state-of-the-art experiments on Si qubits mainly comprise a one-dimensional qubit array<sup>6-9</sup>. Although significant progress has been made since the early stages, this status of spin qubits contrasts with the development of superconducting qubits, wherein advanced institutes and universities are competing by increasing the number of qubits in surface code<sup>10,11</sup>. The advantage of superconducting qubits is their long coherence time despite the relatively large size of the qubits. In contrast, traditional spin qubits require several wires for realizing control and measurement (the "jungle of wiring" problem). This problem may be solved when advanced 2-nm fabrication process technologies become widespread in the commercial phase. We believe that, until then, a realistic application may be required to upgrade spin qubit technologies. In this study, we investigate the application of reservoir computing (RC) using a spin qubit array. RC is a promising recurrent neural network<sup>12-14</sup>. Compared with general recurrent neural networks, the feedbacks of the weight functions are limited to the output part of the network. Thus, the learning speed of RC is higher than that of conventional recurrent neural networks. In addition, various natural physical systems can be used directly in the network. Therefore, various proposals have been made in this regard<sup>15-19</sup>.

According to the development of the aforementioned classical RC, quantum RCs (QRCs) have also been proposed by many researchers<sup>20-23</sup>. Fujii and Nakajima<sup>20,21</sup>

proved the effectiveness of QRC in a nuclear magnetic resonance (NMR) system, wherein the Ising interaction was used. However, we believe that these approaches cannot be applied directly to solid-state silicon qubits from two points. The first problem is regarding the method of inputting the data sequence into a qubit state. Fujii and Nakajima<sup>20,21</sup> and many other researchers determined the input qubit state such that the coefficients of the wave function directly reflected the input data (0 or 1) with the use of a completely positive and trace-preserving (CPTP) map. However, it is difficult to determine the qubit state in spin qubits each time in the input data sequence.

The second problem is regarding the controlled-NOT (CNOT) operation. Yamamoto's group proposed an RC for superconducting qubits, wherein the operations between the qubits were CNOT operations<sup>22,23</sup>. However, in spin qubits, the CNOT gate operations are still "expensive"<sup>25-27</sup>. This is because, in RC, several operations are required but it is unrealistic to use CNOT gates frequently. Therefore, we must determine an appropriate input method that fits the spin qubits.

In this study, we investigate the QRC approach, which is consistent with the current status of spin qubit experiments. We considered spin qubit RC using only pulse sequences for a fixed initial state. The input data, including 0 and 1, are represented by the rotation angle  $\theta_k$  of the  $x$ -axis rotation. Instead of CNOT gates, we use always-on Heisenberg interactions, which can be naturally induced in spin qubit systems.

In an echo-state network (ESN)<sup>12</sup>, the reservoir internal state  $x_k$  at time step  $k$  is a function of  $x_k$  and its previous data  $x_{k-1}$ . This means that the status at the time step  $k$  does not explicitly include the previous data  $x_{k-m}$  for  $m > 1$ . This setting can result in an important behavior of the ESN called the echo state property. However, in a general physical system, the state at  $k$  also depends on those of  $x_{k-m}$  for  $m > 1$ . Thus, we estimate the ESN where the time evolution includes previous states that are more than two steps before.

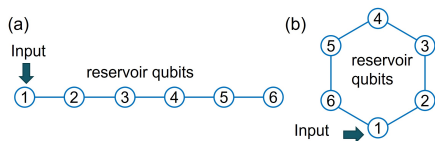


FIG. 1: Reservoir system comprising six spin qubits ( $N_q = 6$ ). (a) Linear arrangement. (b) Circle arrangement. The numbered circles correspond to the spin qubits.

In Ref.<sup>24</sup>, we presented the basic results of our proposed theory. In this study, we extend this theory and present Figs. 4, 5, 6, and 8. The remainder of this paper is organized as follows. The basic formulation of the RC in spin qubit is presented in Section 2. Section 3 presents the consideration of the dissipation. Section 4 presents the numerical results. Section 5 presents a discussion of the results, and Section 6 provides a summary and the conclusions of this study.

## II. RESERVOIR COMPUTING FOR SPIN QUBIT SYSTEM

### A. Previous approach to QRC

In Ref.<sup>20</sup>, the data sequences are input into the first qubit, which is separated from the other parts (input-encoding method). In their method, for the input bit sequence  $s_k$  ( $s_k \in \{0, 1\}$ ), the input qubit is defined, and its quantum state  $|\Psi_{s_k}\rangle^{\text{in}}$  is changed to

$$|\Psi_{s_k}\rangle^{\text{in}} = \sqrt{1 - s_k}|0\rangle + \sqrt{s_k}|1\rangle. \quad (1)$$

Subsequently, the system density matrix is transferred to

$$\rho \rightarrow \rho_{s_k} \otimes \text{Tr}_{\text{in}}\rho, \quad (2)$$

where  $\text{Tr}_{\text{in}}$  denotes the trace with respect to the input qubit. The measurement and feedback are required to form the wavefunction in Eq.(1) (CPTP mapping). However, the CPTP mapping originates from a quantum communication system, and it is unclear how the CPTP map can be satisfied in a noisy solid-state spin qubit system.

The density matrix  $\rho_{k+1}$  at time step  $k+1$  is given by  $\rho_{k+1} = \rho_{\text{in}} \otimes \text{Tr}_1(\rho_k)$ , where  $\rho_{\text{in}}$  denotes the density matrix of the input qubit, and  $\text{Tr}_1$  denotes the partial trace of the input qubit. This scheme exhibited an excellent RC performance in the literature. However, in case of the spin qubits<sup>30</sup>, the spins interact with always-on interactions, and they are controlled only by an external pulsing magnetic field. Thus, it is difficult to separately treat the input qubit from other qubits. Therefore, the use of the input encoding method for spin qubits is unrealistic.

### B. Our approach to QRC using spin qubits

Figure 1 presents the two arrangements of the spin qubit system. We consider the spin qubits system which

interacts via Heisenberg interactions, the Hamiltonian of which is given by

$$H_{\text{int}} = \sum_{i,j}^{N_q} J_{ij}(X_i X_j + Y_i Y_j + Z_i Z_j), \quad (3)$$

where  $X_i$ ,  $Y_i$ , and  $Z_i$  are the Pauli matrices given by

$$X = \begin{pmatrix} 0 & 1 \\ 1 & 0 \end{pmatrix}, \quad Y = \begin{pmatrix} 0 & -i \\ i & 0 \end{pmatrix}, \quad Z = \begin{pmatrix} 1 & 0 \\ 0 & -1 \end{pmatrix}, \quad (4)$$

(We set  $\hbar = 1$  and the number of qubits as  $N_q = 6$ ). On solving the eigenvalue problem, the wavefunction is obtained as  $|\psi_k\rangle$ , and the unitary matrix is given by

$$U_{\text{int}}(t) = \exp(-itH_{\text{int}}). \quad (5)$$

In the following calculations,  $J_{ij}$  is randomly selected as  $0 \leq J_{ij} \leq 1$  (we set the energy scale as  $\max(J_{ij}) = 1$ ). On assuming a large applied static magnetic field, each electron has the two states of spin-up and spin-down owing to the Zeeman splitting (two-level state). The input data sequence  $s_k$  is considered as the rotation angle around the  $X$  axis and is given by

$$R_X(s_k) = \exp(i\pi s_k X_1/2), \quad (6)$$

(the rotating wave approximation is assumed)<sup>31</sup>. The system evolves using the unitary operator  $U(t)$  given by  $U(t) = \Pi_k R_X(s_k) U_k$ , where  $U_k = \exp(-i\Delta t H_{\text{int}})$  where  $\Delta t = \pi\theta_0$ . Although we attempted to use different values of  $\theta_0$ , we typically considered  $\theta_0 = 0.5$  for the following calculations.

The nondemolition measurements are assumed, and the six qubit states are unaffected by the measurements. In the measurement of a standard spin qubit system, the Pauli spin blockade is used<sup>29</sup>. In a Pauli-spin-blockade-based quantum dot system, each qubit accompanies an additional quantum dot, where an additional quantum dot state is measured by single-electron transistors (see the discussion below). We assume that the  $Z$ -measurement is conducted using the measurement. The measurement result  $\langle Z_i \rangle$  is described by a density matrix  $\rho(t)$  given by

$$\langle Z_i \rangle = \text{Tr} Z_i \rho(t). \quad (7)$$

The entire process consists of  $N_{\text{pre}}$  preparation steps,  $N_{\text{fb}}$  learning steps, and  $N_{\text{test}}$  testing steps (where  $N_{\text{pre}} = N_{\text{fb}} = 200$ , and  $N_{\text{test}} = 40$ ).

There are two options for selecting the reservoir outputs. Lee and Mochizuki<sup>28</sup> demonstrated that the  $Z$ -component magnetization of a skyrmion averaged over sites exhibits a good performance. The direct use of six qubit measurements is another candidate. Thus, we consider two types of relationships between the measurement results and the reservoir outputs ( $y_k^{\text{I}}$  and  $y_k^{\text{II}}$ ). In the first type  $y_k^{\text{I}}$ ,  $N_q$  measurement results  $x_{ki} = \langle Z_i \rangle$ , are used and given by  $y_k^{\text{I}} = \sum_{i=0}^{N_q} x_{ki} w_i$ , where  $w_i$  is the read-out weight ( $i = 0, \dots, N_q$ ), and  $x_0 = 1$  is a constant. In

the second type, the average measurement result used is  $x_k = \frac{1}{N_q} \sum_{i=1}^{N_q} \langle Z_i \rangle$ , and  $y_k^{\text{II}}$  is given by  $y_k^{\text{II}} = x_0 w_0 + x_k w_1$ , where  $x_0 = 1$  and  $w_i$  are the readout weight. Both the reservoir outputs were determined by minimizing the  $\sum_k |y_k - \bar{y}_k|^2$  for the target output  $\bar{y}$ . In the test phase,  $y_k$  is predicted as  $y_k^{\text{pred}} = \sum_i x_{ki} w_i$  for  $x_{ki}$  in the test region.

Here, the short-term memory (STM) and nonlinear autoregressive moving average (NARMA) tasks are studied. The STM task is evaluated as the time delay  $\tau_B$  given by

$$y_k = s_{k-\tau_B}, \quad (8)$$

which characterizes the ability of the STM<sup>20</sup>. The input of the NARMA task is given as

$$s_k = 0.1 \left[ \sin\left(\frac{2\pi\alpha_0 k}{T}\right) \sin\left(\frac{2\pi\alpha_1 k}{T}\right) \sin\left(\frac{2\pi\alpha_2 k}{T}\right) + 1 \right], \quad (9)$$

where  $(\alpha_0, \alpha_1, \alpha_2) = (2.11, 3.73, 4.11)$  and  $T = 100$ . The error is estimated using the standard normalized mean squared error (NMSE)<sup>19,20</sup> given by

$$\text{NMSE} = \frac{\sum_{k=L+1}^M (\bar{y}_{k+1} - y_{k+1})^2}{\sum_{k=L+1}^M \bar{y}_{k+1}^2}, \quad (10)$$

where  $L = N_{\text{prep}} + N_{\text{fb}}$  denotes the number of time steps until the training phase, and  $M = L + N_{\text{test}}$  denotes the number of time steps until the evaluation phase.

### III. DISSIPATION

The echo-state property requires STM, but not long-term memory. In a physical system, this implies that the dissipation is strong. We then include the dissipation as follows. The two qubit states  $|0\rangle$  and  $|1\rangle$  are defined as the spin-down and spin-up states, assuming a strong  $z$ -directional magnetic field. We assume that dissipations occur owing to various noises, and the excited state  $|1\rangle$  decays to the ground state  $|0\rangle$  with a decay rate  $\gamma$ . The evolution of the density matrix can then be expressed as

$$\rho_{k+1} = U_k \rho_k U_k^\dagger (1 - \gamma) + \gamma \rho_0, \quad (11)$$

where  $\rho_0 \equiv |0, \dots, 0\rangle\langle 0, \dots, 0|$ . Although we attempted to use several wavefunctions, no significant differences were observed between them. Thus, the following calculations are performed, starting from the initial state  $|0, \dots, 0\rangle$  at a time step of 0.

### IV. RESULTS

Figure 2 presents the results of the STM tests for types I and II, where  $C_{\text{STM}}(\tau_B)$  is the STM capacity and is given by the square of the correlation coefficients of  $y_k$  and  $\bar{y}_k$ . Because the number of weights  $w_i$  in type I is greater than that of the type II, the former exhibited a

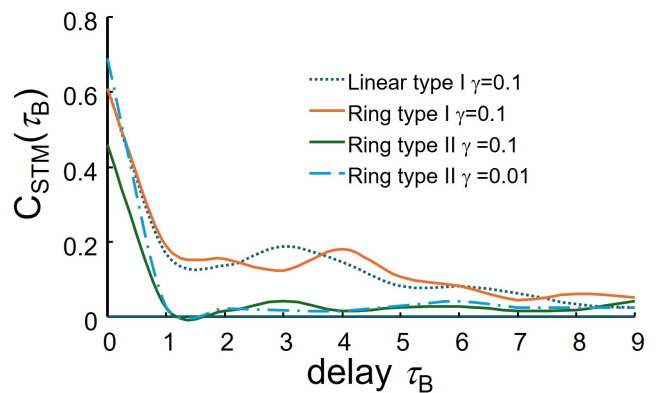


FIG. 2: STM tests for the linear and ring arrangement of Fig.1 for  $\gamma = 0.1$  and  $\gamma = 0.01$ .

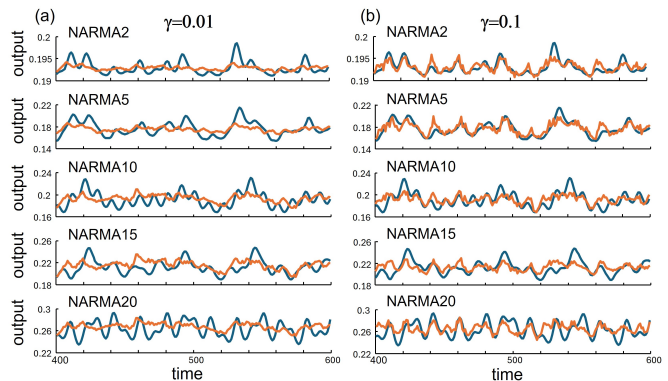


FIG. 3: Typical example of linear structure (Fig.1(a)) for the NARMA tasks for  $\gamma = 0.01$  (left column) and  $\gamma = 0.1$  (right column) in type I. The dark-cyan and orange lines indicate the target and reservoir outputs, respectively.

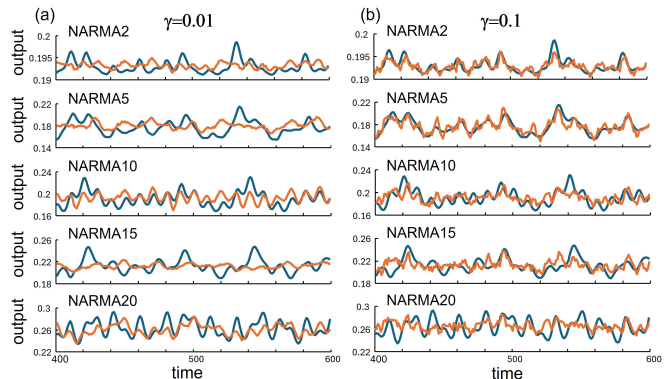
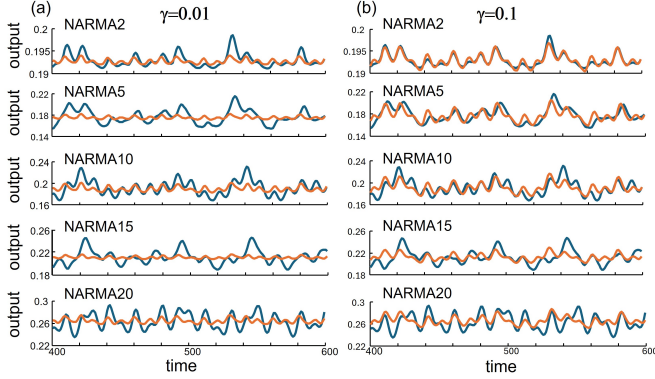
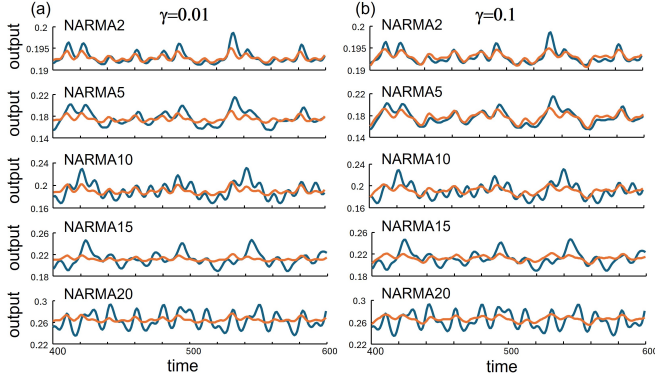


FIG. 4: Typical example of ring structure (Fig.1(b)) for the NARMA tasks for  $\gamma = 0.01$  (left column) and  $\gamma = 0.1$  (right column) in type I. The dark-cyan and orange lines indicate the target and reservoir outputs, respectively.

TABLE I: NMSE in NARMA tasks of two  $\gamma$ s for a type I and type II qubit array.

	Type I				Type II			
	$\gamma=0.1$	$\gamma=0.01$	$\gamma=0.1$	$\gamma=0.01$	$\gamma=0.1$	$\gamma=0.01$	$\gamma=0.1$	$\gamma=0.01$
NARMA2	2.25E-05	5.76E-05	2.58E-05	7.00E-05	7.45E-06	5.01E-05	6.52E-06	4.01E-05
NARMA5	1.76E-03	6.17E-03	1.81E-03	6.74E-03	1.81E-03	6.26E-03	2.17E-03	5.66E-03
NARMA10	3.65E-03	6.12E-03	3.37E-03	5.88E-03	4.18E-03	6.13E-03	3.88E-03	5.55E-03
NARMA15	4.37E-03	4.35E-03	4.05E-03	4.13E-03	4.72E-03	4.76E-03	4.82E-03	4.73E-03
NARMA20	3.07E-03	2.83E-03	3.35E-03	2.99E-03	3.13E-03	2.92E-03	3.16E-03	2.87E-03

FIG. 5: Typical example of the linear structure (Fig.1(a)) for the NARMA tasks for  $\gamma = 0.01$  (left column) and  $\gamma = 0.1$  (right column) in type II. The dark-cyan and orange lines indicate the target and reservoir outputs, respectively.FIG. 6: Typical example of ring structure (Fig.1(b)) for the NARMA tasks for  $\gamma = 0.01$  (left column) and  $\gamma = 0.1$  (right column) in type II. The dark-cyan and orange lines indicate the target and reservoir outputs, respectively.

superior performance. The linear cases for the other patterns are not presented here because they show smaller STM capacities. Figures 3–6 present examples of the NARMA tests for both types I and II with linear and ring structures. Table I lists the results of the NARMA tests for types I and II. The NARMA2 and NARMA5 tasks yielded relatively good results in both cases. In both types, the larger- $\gamma$  cases exhibited better perfor-

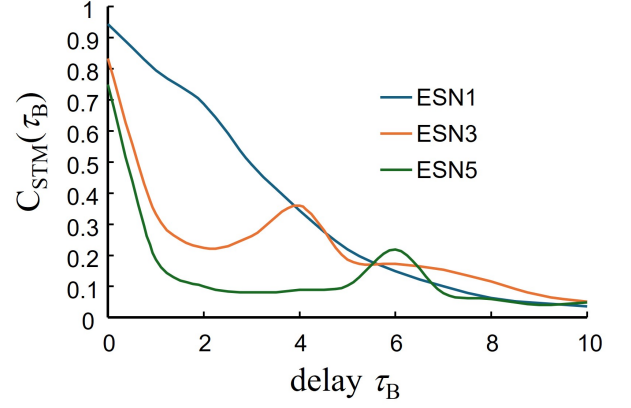


FIG. 7: STM test for the ESN for long correlations.

mances. This indicates that the dissipation process is important in QRC, which is similar to the case of conventional RC. A small  $\gamma$  value indicates that the system remembers the previous events. However, this long memory disturbs the newly inputted sequences. In Ref. <sup>18</sup>, the soft silicone arm appears to remember only a few of its previous steps. The memory of the soft silicone arm disappears in the resistance to water. On comparing Figs. 3 and 4 with Figs. 5 and 6, the typical waveform of type II appears slightly better than that of type I.

Our results suggest that a smaller dissipation induces poor performance in our QRCs. To confirm whether a similar relationship is satisfied even in an ESN<sup>12</sup>, we modified the ESN function as follows

$$x_{ki} = \tanh\left(\sum_j w_{ij}(x_{k-1,j} + x_{k-3,j} + x_{k-5,j}) + w_{in,i}s_k\right), \quad (12)$$

for the reservoir output  $y_k = \sum_i w_{out,i}x_{ki}$  (ESN5). Here, we consider a uniformly random  $w_{ij}$  between 0 and 0.4. For ESN3 and ESN1, the terms after  $w_{ij}$  are replaced by  $x_{k-1,j} + x_{k-3,j}$  and  $x_{k-1,j}$ , respectively. Figure 7 and Table II present the results of these long correlations of the ESN. For longer correlations (ESN3 and ESN5), the STM task yielded a poorer performance. However, Table II shows that there is no significant difference between the NARMA tasks for ESN1, ESN3, and ESN5. This tendency is the same as that of the spin qubit system. Thus, it could be said that the ESN in Ref.<sup>12</sup> corresponds to a

TABLE II: NMSE in NARMA tasks for ESN of long correlations.

	ESN1	ESN3	ESN5
NARMA2	9.85E-04	9.64E-04	2.22E-04
NARMA5	1.98E-03	3.59E-03	1.61E-02
NARMA10	2.74E-03	4.00E-03	1.47E-02
NARMA15	3.48E-03	3.49E-03	7.45E-02

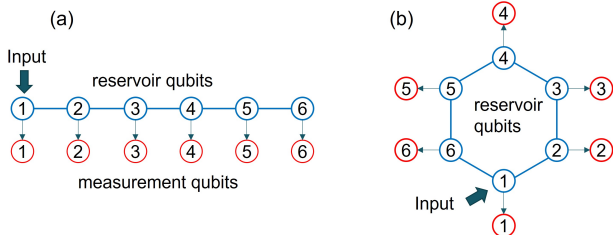


FIG. 8: Positions of the ancillary qubits (measurement qubits) for both the linear and ring structures.

strong-dissipation case of the physical system.

## V. DISCUSSIONS

We assumed that the measurements were performed without disturbing the reservoir qubit system. This situation can be realized by adding ancillary qubits as shown in Fig.8. The ancillary qubits are placed outside the reservoir qubits. In traditional gate-defined qubits<sup>6-9</sup>, the qubits and wires are placed in the same plane. In the case of linear structures, both the reservoir and ancillary qubits can be accessed from the other side of the qubit-qubit coupling. In contrast, in a ring structure, the access lines to the reservoir qubits are limited between the ancillary qubits. Thus, from the viewpoint of fabrication,

linear qubits are more feasible. Other than the use of the Pauli spin blockade, the CNOT operation from the reservoir qubit to the measurement qubit can be applied in the context of conventional quantum computations.

In this study, we performed the STM and NARMA tasks. To estimate the qubit reservoir, other benchmark tasks such as the parity-check and timer tasks should be applied. These issues will be required to be addressed in future studies. Herein, the number of qubits used was six. We also estimated the STM and NARMA tasks for the  $N_q = 4$  case; however, a worse performance (not shown herein) was observed compared to those presented in this study. Despite the significant computational cost involved, the case of larger number of qubits will be investigated in the near future.

## VI. CONCLUSIONS

We theoretically investigated an RC system using a spin qubit array in this study. Compared with the input encoding method, wherein the input sequence is exactly implemented in the first qubit, decoherence prevails over all the qubits herein. Nevertheless, the NARMA tests yielded relatively good results and demonstrated that the QRC in the spin qubit array is promising as an application of spin qubits. The detailed comparison of the QRC with other RC systems will be focused on in a future study.

## Acknowledgments

We are grateful to K. Ono for the fruitful discussions we had. This study was supported by JSPS KAKENHI Grant Number JP22K03497. This study was also partially supported by the MEXT Quantum Leap Flagship Program (MEXT Q-LEAP; Grant Number JP-MXS0118069228), Japan.

<sup>1</sup> D. Loss and D. P. DiVincenzo, Phys. Rev. A **57**, 120 (1998).  
<sup>2</sup> A. G. Fowler, M. Mariantoni, J.M. Martinis, and A.N. Cleland, Phys. Rev. A **86**, 032324 (2012).  
<sup>3</sup> C. D. Hill, E. Peretz, S. J. Hile, M. G. House, M. Fuechsle, S. Rogge, M. Y. Simmons, and L. C.L. Hollenberg, Sci. Adv. **1**, e1500707 (2015).  
<sup>4</sup> M. Veldhorst, H. G. J. Eenink, C. H. Yang, and A. S. Dzurak, Nat. Commun. **8**, 1766 (2017).  
<sup>5</sup> T. Tanamoto and K. Ono, J. Appl. Phys. **134**, 214402 (2023).  
<sup>6</sup> S. Neyens, O. K. Zietz, T. F. Watson, F. Luthi, A. Nethewala, H. C. George, E. Henry, M. Islam, A. J. Wagner, F. Borjans, E. J. Connors, J. Corrigan, M. J. Curry, D. Keith, R. Kotlyar, L. F. Lampert, M. T. Madzik, K. Millard, F. A. Mohiyaddin, S. Pellerano, R. Pillarisetty, M. Ramsey, R. Savytsky, S. Schaal, G. Zheng, J. Ziegler, N. C. Bishop, S. Bojarski, J. Roberts, and J. S. Clarke, Nature **629**, 80

(2024).  
<sup>7</sup> J. Y. Huang, R. Y. Su, W. H. Lim, M. Feng, B. van Straaten, B. Severin, W. Gilbert, N. D. Stuyck, T. Tanttu, S. Serrano, J. D. Cifuentes, I. Hansen, A. E. Seedhouse, E. Vahapoglu, R. C. C. Leon, N. V. Abrosimov, H.-J. Pohl, M. L. W. Thewalt, F. E. Hudson, C. C. Escott, N. Ares, S. D. Bartlett, A. Morello, A. Saraiva, A. Laucht, A. S. Dzurak, and C. H. Yang, Nature **627**, 772 (2024).  
<sup>8</sup> B. Undseth, O. Pietx-Casas, E. Raymenants, M. Mehmandoust, M. T. Madzik, S. G. J. Philips, S. L. de Snoo, D. J. Michalak, S. V. Amitonov, L. Tryputen, B. P. Wuetz, V. Fezzi, D. D. Esposti, A. Sammak, G. Scappucci, and L.M.K. Vandersypen, Phys. Rev. X **13**, 041015 (2023).  
<sup>9</sup> K. Takeda, A. Noiri, T. Nakajima, L. C. Camenzind, T. Kobayashi, A. Sammak, G. Scappucci, and S. Tarucha, npj Quantum Inf. **10**, 22 (2024).  
<sup>10</sup> Google Quantum AI, Nature **614**, 676 (2023).  
<sup>11</sup> D. Castelvecchi, Nature **624**, 238 (2023).

- <sup>12</sup> H. Jaeger and H. Haas, *Science* **304**, 78 (2004).
- <sup>13</sup> W. Maass, T. Natschlagel, and H. Markram, *Neural Comput.* **14**, 2531 (2002).
- <sup>14</sup> D. Verstraeten, B. Schrauwen, M. DHaene, and D. Stroobandt, *Neural Netw.* **20**, 391 (2007).
- <sup>15</sup> S. Iihama, Y. Koike, S. Mizukami, and N. Yoshinaga, *npj Spintronics* **2**, 5 (2024).
- <sup>16</sup> R. Nakane, G. Tanaka, and A. Hirose, *IEEE Access* **6**, 4462 (2018).
- <sup>17</sup> E. Nako, K. Toprasertpong, R. Nakane, M. Takenaka, and S. Takagi, 2022 IEEE Symposium on VLSI Technology and Circuits (VLSI Technology and Circuits), Honolulu, HI, USA, (2022).
- <sup>18</sup> K. Nakajima, H. Hauser, T. Li, and R. Pfeifer, *Sci. Rep.* **5**, 10487 (2015).
- <sup>19</sup> T. Kanao, H. Suto, K. Mizushima, H. Goto, T. Tanamoto, and T. Nagasawa, *Phys. Rev. Appl.* **12**, 024052 (2019).
- <sup>20</sup> K. Fujii and K. Nakajima, *Phys. Rev. Appl.* **8**, 024030 (2017).
- <sup>21</sup> K. Nakajima, K. Fujii, M. Negoro, K. Mitarai, and M. Kitagawa, *Phys. Rev. Appl.* **11**, 034021 (2019).
- <sup>22</sup> Y. Suzuki, Q. Gao, K. C. Pradel, K. Yasuoka, and N. Yamamoto, *Sci. Rep.* **12**, 1353 (2022).
- <sup>23</sup> T. Yasuda, Y. Suzuki, T. Kubota, K. Nakajima, Q. Gao, W. Zhang, S. Shimono, H. I. Nurdin, and N. Yamamoto, arXiv:2310.06706.
- <sup>24</sup> S. Mifune, T. Kanao, and T. Tanamoto, 2024 Int. Conf. Solid State Devices and Materials (SSDM24), Himeji, Japan.
- <sup>25</sup> M. Veldhorst, C. H. Yang, J. C. C. Hwang, W. Huang, J. P. Dehollain, J. T. Muhonen, S. Simmons, A. Laucht, F. E. Hudson, K. M. Itoh, A. Morello, and A. S. Dzurak, *Nature* **526**, 410 (2015).
- <sup>26</sup> K. Takeda, A. Noiri, T. Nakajima, T. Kobayashi, and S. Tarucha, *Nature* **608**, 682 (2022).
- <sup>27</sup> D. M. Zajac, A. J. Sigillito, M. Russ, F. Borjans, J. M. Taylor, G. Burkard, and J. R. Petta, *Science* **359**, 439 (2017).
- <sup>28</sup> M.-K. Lee and M. Mochizuki, *Phys. Rev. Appl.* **18**, 014074 (2022).
- <sup>29</sup> K. Ono, D. G. Austing, Y. Tokura, and S. Tarucha, *Science* **297**, 1313 (2002).
- <sup>30</sup> K. Takeda, A. Noiri, T. Nakajima, T. Kobayashi, and S. Tarucha, *Nature* **608**, 682 (2022).
- <sup>31</sup> S. Kobayashi, Q. Ho. Tran, and K. Nakajima, arXiv:2403.02686.